

On the methanol emission detection in the TW Hya disc: the role of grain surface chemistry and non-LTE excitation

S. Yu. Parfenov,^{1*} D. A. Semenov,² Th. Henning,² A. S. Shapovalova,¹ A. M. Sobolev,¹ R. Teague²

¹*Ural Federal University, 51 Lenin Str., Ekaterinburg 620000, Russia*

²*Max Planck Institute for Astronomy, Königstuhl 17, D-69117 Heidelberg, Germany*

Accepted XXX. Received YYY; in original form ZZZ

ABSTRACT

The recent detection of gas-phase methanol (CH_3OH) lines in the disc of TW Hya by Walsh et al. provided the first observational constraints on the complex O-bearing organic content in protoplanetary discs. The emission has a ring-like morphology, with a peak at $\sim 30 - 50$ au and an inferred column density of $\sim 3 - 6 \times 10^{12} \text{ cm}^{-2}$. A low CH_3OH fractional abundance of $\sim 0.3 - 4 \times 10^{-11}$ (with respect to H_2) is derived, depending on the assumed vertical location of the CH_3OH molecular layer. In this study, we use a thermo-chemical model of the TW Hya disc, coupled with the *ALCHEMIC* gas-grain chemical model, assuming laboratory-motivated, fast diffusivities of the surface molecules to interpret the CH_3OH detection. Based on this disc model, we performed radiative transfer calculations with the *LIME* code and simulations of the observations with the *CASA* simulator. We found that our model allows to reproduce the observations well. The CH_3OH emission in our model appears as a ring with radius of ~ 60 au. Synthetic and observed line flux densities are equal within the rms noise level of observations. The synthetic CH_3OH spectra calculated assuming local thermodynamic equilibrium (LTE) can differ by up to a factor of 3.5 from the non-LTE spectra. For the strongest lines, the differences between LTE and non-LTE flux densities are very small and practically negligible. Variations in the diffusivity of the surface molecules can lead to variations of the CH_3OH abundance and, therefore, line flux densities by an order of magnitude.

Key words: astrochemistry – line: formation – molecular processes – protoplanetary discs – sub-millimetre: planetary systems – stars: individual: TW Hya.

1 INTRODUCTION

The architecture of planetary systems and the composition of extrasolar planets appear to be tightly linked with the structure and chemical evolution of their birth sites, protoplanetary discs (Mordasini et al. 2012a,b; Winn & Fabrycky 2015). The disc chemical composition may additionally shape the properties of exoplanetary atmospheres (e.g. Bergin et al. 2015; Cridland et al. 2016; Mordasini et al. 2016). Furthermore, some of complex organic (pre-biotic) molecules in the primordial planetary atmospheres may be formed during the natal disc evolution (see e.g. Ciesla & Sandford 2012; Caselli & Ceccarelli 2012; Henning & Semenov 2013). The results from the recent *ROSETTA* mission to the comet 67P/Churyumov-Gerasimenko indicate that highly complex

organic molecules, including methanol, were present at the verge of planet formation in the solar nebula and could have been later delivered on early Earth during the Late Heavy Bombardement phase (Biver et al. 2015; Fray et al. 2016).

So far, however, there were only a few organic species with O- or N-atoms have been detected in discs, namely, H_2CO (Aikawa et al. 2003), HCN , HNC , HC_3N (Chapillon et al. 2012), and CH_3CN (Öberg et al. 2015). Despite intense searches, methanol emission was not detected in discs until recently (Walsh et al. 2016, hereafter W16). CH_3OH is mainly synthesized via surface chemistry associated with CO and plays an important role in the formation of more complex organic species (see e.g. Herbst & van Dishoeck 2009). The study of Drozdovskaya et al. (2014) showed that the methanol ice in the outer disc regions may be inherited from the parental clouds in the prestellar stage. These clouds have detectable amounts of the methanol both in gas

* E-mail: sergey.parfenov@urfu.ru

phase Kalenskii & Sobolev (1994) and on the grain surface Gürtler et al. (2002). The capacity of the methanol reservoir within the grain mantles can be demonstrated by the fact that release of the methanol from the grain mantles can increase the gas-phase abundance of this molecule, X_M (wrt H_2), by many orders of magnitude Sutton et al. (2004). The methanol gas-phase abundance predicted by different chemical disc models varies by orders of magnitude (see e.g. Walsh et al. 2014), with the main source of uncertainty in X_M being due to the poorly known chemical reaction rates (see e.g. Vasyunin et al. 2008) and the binding and desorption energies of ices. Furthermore, the CH_3OH lines in discs can be subject to non-local thermodynamic equilibrium (non-LTE) excitation and thus a full non-LTE line radiative transfer (LRT) modelling is necessary (Parfenov et al. 2016).

The detection of CH_3OH emission in the disc of TW Hya by W16 is a great achievement in the characterization of the chemical complexity in protoplanetary discs. W16 estimated $X_M \sim 0.3\text{--}4 \times 10^{-11}$ utilising the disc physical model of Kama et al. (2016) and a parametrized CH_3OH spatial distribution. This estimate is lower by two orders of magnitude than those predicted by contemporary chemical models of T Tauri discs. Such an inconsistency can be related to both the incompleteness of chemical models and the differing disc structure of TW Hya to the discs structures typically adopted for disc chemical modelling (by e.g. Willacy 2007; Semenov & Wiebe 2011; Walsh et al. 2014; Furuya & Aikawa 2014).

In this paper, we continue our study of complex organic chemistry and line excitation in discs. We interpret the CH_3OH emission detection using a physical model of the TW Hya disc coupled with a complex chemical model (Section 2). The CH_3OH distribution computed with this disc model is used for non-LTE and LTE LRT calculations (Section 3). Based on the results of LRT calculations we simulate observations of the TW Hya disc with the Atacama Large Millimeter/submillimeter Array (ALMA) and compare these simulated observations with W16 results (Section 4). A discussion and conclusions follow.

2 TW HYA DISC MODEL

For the physical structure of the TW Hya disc, we adopted the thermo-chemical model from Gorti et al. (2011). This model is based on the iterative fitting of multiple gas emission spectra and dust emission data ranging from the sub-millimetre to the optical wavelengths. The dust model is taken from Calvet et al. (2002) and has a total dust mass of $2.4 \times 10^{-4} M_\odot$, following a grain size distribution $n(a) \propto a^{-3.5}$ with a maximum grain size $a_{\max} = 1$ mm. The assumed polycyclic aromatic hydrocarbons abundance per H atom is $\sim 10^{-9}$. A constant dust-to-gas mass ratio of 100 is assumed. An accretion rate of $10^{-9} M_\odot \text{ yr}^{-1}$ is assumed. The disc model spans 3.9–200 au radially and has separately computed gas and dust temperatures. To compute the gas thermal balance, a concise chemistry model with ~ 85 species and ~ 600 reactions is utilized.

The adopted parameters of the central star and the incident ultraviolet (UV) and X-ray radiation fields represent those observed in TW Hya. The star has a mass of $0.7 M_\odot$, a radius of $1 R_\odot$, and an effective temperature of 4200 K.

A detailed far-UV spectrum with a total far-UV luminosity of $3 \times 10^{31} \text{ erg s}^{-1}$ was used. The adopted X-ray spectrum, covering 0.1–10 keV, has a total X-ray luminosity of $1.6 \times 10^{30} \text{ erg s}^{-1}$.

The chemical structure of the disc was computed with the gas-grain code ALCHEMIC described in detail by Semenov et al. (2010); Semenov & Wiebe (2011) and used in our previous methanol study, Parfenov et al. (2016). A new lower ultraviolet-photodesorption yield of 10^{-5} is adopted for all species, based on the recent measurements of Cruz-Diaz et al. (2016) and Bertin et al. (2016). While the inferred age of the TW Hya system is about 7 Myr (Ducourant et al. 2014), we modelled the disc chemical evolution over only 1 Myr. This was dictated by the slow performance of our gas-grain code, limited by the very slow pace of surface processes on $7 \mu\text{m}$ -sized grains. We note that CH_3OH abundances are in a quasi-steady state at 0.2–1 Myr in the disc regions with high CH_3OH abundances ($X_M \gtrsim 10^{-12}$).

In our model, CH_3OH is formed on dust surfaces via the hydrogenation of CO, in which hydrogen tunnelling through reaction barriers is taken into account, however tunnelling through potential wells of surface sites is neglected. Additionally, CH_3OH can be formed on dust surfaces via radical-radical recombination between OH and CH_3 , which in turn are formed by surface recombination reactions and UV photoprocessing of more complex ‘parent’ molecules. CH_3OH can also be formed inefficiently in the gas phase via dissociative recombination of $CH_3OH_2^+$ with e^- , which, in our network, has a 5 per cent probability to produce CH_3OH and H. The methanol in our model is released into the gas-phase mainly through chemical desorption and photodesorption of the CH_3OH ice by UV radiation (see Fig. 1). Both the interstellar UV and the secondary UV radiation produced by the cosmic ray particle (CRP) excitation of H_2 are important. The peak temperature of the grain particle due to the impulsive heating from CRPs is estimated taking into account an initial grain temperature with equation (6) from Semenov et al. (2004) and is relatively low comparing with methanol desorption energy (5530 K). Thus, CRP induced desorption through the grain heating is ineffective in our model. Chemical desorption, with an efficiency of 1 per cent, occurs for all surface recombination reactions, including CH_3OH formation.

The values of X_M used in Parfenov et al. (2016) were computed for a solar nebula model from Semenov & Wiebe (2011) and are lower by about two orders of magnitude compared to the chemical model of similar complexity from Walsh et al. (2014). As noted in Parfenov et al. (2016), this discrepancy can be due to the relatively low grain-surface diffusion rates assumed by Semenov & Wiebe (2011), with the ratio of diffusion to binding energy E_{diff}/E_b of 0.77 for surface species. In this study, however, we consider surface reactions with faster diffusion rates with $E_{\text{diff}}/E_b = 0.4$, close to the $E_{\text{diff}}/E_b = 0.3$ used by Walsh et al. (2014). A value of $E_{\text{diff}}/E_b = 0.4$ is more consistent with the recent laboratory studies of Cuppen et al. (2017). In order to see how the disc chemical composition can be affected by the uncertainties of E_{diff}/E_b we also performed calculations with $E_{\text{diff}}/E_b = 0.77$. Our models with $E_{\text{diff}}/E_b = 0.77$ and 0.4 will be denoted as ‘ $E_{\text{diff}}/E_b = 0.77$ ’ and ‘ $E_{\text{diff}}/E_b = 0.4$ ’ models, respectively.

In both ‘ $E_{\text{diff}}/E_b = 0.77$ ’ and ‘ $E_{\text{diff}}/E_b = 0.4$ ’ chemical models, gas-phase CH_3OH resides mainly in the disc re-

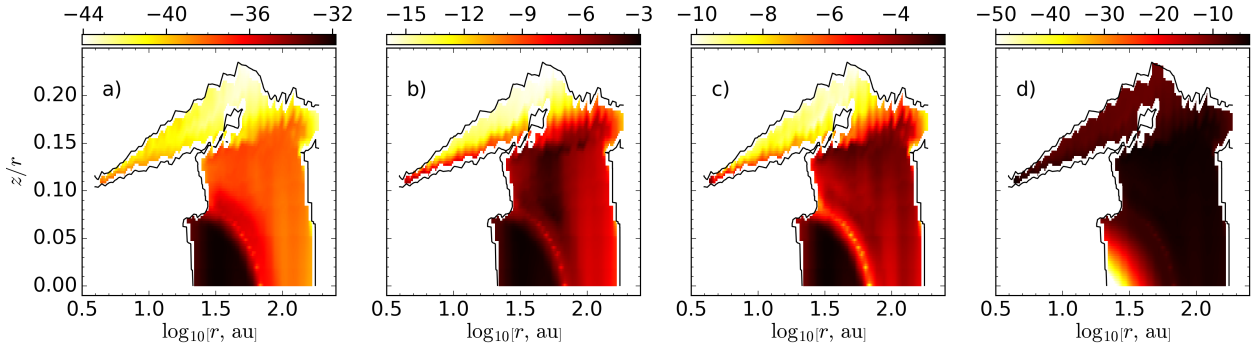


Figure 1. The log of methanol desorption rates in $\text{cm}^{-3} \text{s}^{-1}$ estimated for the ‘ $E_{\text{diff}}/E_b = 0.4$ ’ disc model. The rates are shown only in the disc regions with $X_M > 10^{-15}$. (a) CRP desorption rate. (b) Reactive desorption rate. (c) Photodesorption rate. (d) Photodesorption rate estimated without taking into account the secondary UV photons produced by CRP excitation of H_2 . The black contours denote the gas-phase CH_3OH abundance of 10^{-15} .

gions with $z/r < 0.25$ (see Fig. 2), where z denotes the height above the disc mid-plane and r is the distance from the disc centre. This is in good agreement with the spatial distribution of CH_3OH considered by W16. The maximum CH_3OH abundance, X_{0M} , in ‘ $E_{\text{diff}}/E_b = 0.77$ ’ and ‘ $E_{\text{diff}}/E_b = 0.4$ ’ models is comparable: 1.87×10^{-10} and 1.55×10^{-10} , respectively. However, the gas-phase CH_3OH in the ‘ $E_{\text{diff}}/E_b = 0.4$ ’ model occupies a much larger region of the disc, including the disc mid-plane, in contrast to the ‘ $E_{\text{diff}}/E_b = 0.77$ ’ model. This leads to a difference of several orders of magnitude in CH_3OH vertical column densities, N_M , between ‘ $E_{\text{diff}}/E_b = 0.77$ ’ and ‘ $E_{\text{diff}}/E_b = 0.4$ ’ models for the disc regions with $r < 20$ and $r > 50$ au (see Fig. 2). For example, $N_M = 9 \times 10^{10}$ and $7.1 \times 10^{11} \text{ cm}^{-2}$ at $r = 60$ au for ‘ $E_{\text{diff}}/E_b = 0.77$ ’ and ‘ $E_{\text{diff}}/E_b = 0.4$ ’ models, respectively.

The disc physical structure used in this study is different from the one of Kama et al. (2016) adopted by W16. As can be clearly seen in Figure 3, the Kama et al. disc is denser and colder compared to the disc model of Gorti et al. (2011). To assess how the differences between adopted disc physical models affect the predicted CH_3OH line flux densities, we performed LRT calculations with our disc physical model but using the parametrized CH_3OH distribution considered by W16. It is worth noting that the Gorti et al. (2011) disc model does not have separated mm- and μm -sized grain populations (see e.g. Menu et al. 2014). Both the Gorti et al. (2011) and Kama et al. (2016) disc models do not take into account the gaps seen in scattered light and in the ALMA (sub-)mm images (see e.g. Debes et al. 2013; van Boekel et al. 2016; Andrews et al. 2016). These gaps can be associated with the deficit of large (~ 10 mm) dust grains (Tsukagoshi et al. 2016) or a local gas density depletion (Teague et al. 2017).

3 RADIATIVE TRANSFER CALCULATIONS

For the LRT calculations, we have used the LIne Modelling Engine (LIME) (Brinch & Hogerheijde 2010) and the ‘ $v_t = 0$ ’ CH_3OH level scheme of Parfenov et al. (2016) that is very similar to the one given in the Leiden Atomic and Molecular Database (LAMDA, Schöier et al. 2005). We assumed that A and E species of CH_3OH are equally abundant.

We used the dust opacities from Menu et al. (2014) for

our LRT calculations. As W16 do not state explicitly which dust opacities they used, it makes a comparison of the results between W16 LRT calculations and our test calculations with the W16 CH_3OH parametrized distribution more difficult. To check how the variations in dust opacities can affect the results of our test LRT calculations we performed these calculations using dust opacities from both Menu et al. (2014) and Andrews et al. (2011). The latter dust opacities are consistent with those utilized in DALI code (Bruderer 2013), which in turn have been used by Kama et al. (2016) to construct the model of TW Hya disc. At frequencies of ~ 305 GHz, Menu et al. (2014) dust opacity is higher by about a factor of ~ 1.8 than the one of Andrews et al. (2011).

The spatial grid of 1000000 points used for LRT calculation consisted of 5 subsets of points, each including 200000 points. The positions of points in three of these subsets were selected from weighted random distributions with weighting functions $(n_{\text{H}_2}/n_{0\text{H}_2})^{0.3}$, $(X_M/X_{0M})^{0.3}$ and $[(X_M n_{\text{H}_2})/(X_{0M} n_{0\text{H}_2})]^{0.3}$, where $n_{0\text{H}_2} = 4.2 \times 10^{12} \text{ cm}^{-3}$ is the maximum value of H_2 density, n_{H_2} . These 3 subsets trace the disc regions with high gas and CH_3OH densities. The remaining 2 subsets were constructed to trace the disc regions with relatively low gas density and X_M . The positions of points in these 2 subsets were sampled from random distribution that are uniform in Cartesian coordinates (x, y, z) and in $\log_{10}(\sqrt{x^2 + y^2 + z^2})$, respectively.

The synthetic images in CH_3OH lines were obtained with a pixel size of 0.01 arcsec, which allows us to well resolve the $\sim 1'' \times 1''$ beam, comparable to the one in W16. As in W16, the synthetic images were obtained with a spectral resolution of 0.15 km s^{-1} , assuming a disc inclination and position angle of 7 and 155° (Qi et al. 2004), respectively. We adopted a distance to the TW Hya disc of 59.5 pc from the first Gaia data release (Gaia Collaboration et al. 2016). For consistency with W16, the test calculations with the Gorti et al. (2011) disc model and parametrized CH_3OH distribution of W16 were performed assuming a distance of 54 pc. By adding line specific intensities in the all pixels of the synthetic images, we obtained the synthetic integrated CH_3OH spectra.

LIME produces images at a single spectral frequency without taking into account the averaging within the spectral channels as in real observations. We have checked how

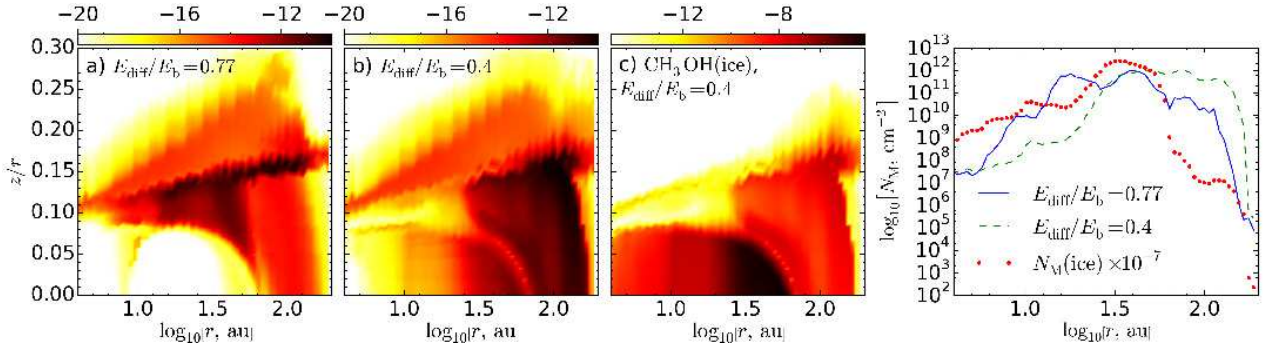


Figure 2. (a) and (b) The log of relative gas-phase CH₃OH abundance with respect to the H₂ density in the ‘ $E_{\text{diff}}/E_b = 0.77$ ’ and ‘ $E_{\text{diff}}/E_b = 0.4$ ’ disc models. (c) Same as (b) but for grain surface (ice) CH₃OH. The most right panel shows gas-phase CH₃OH vertical column density in the ‘ $E_{\text{diff}}/E_b = 0.77$ ’ (solid line) and ‘ $E_{\text{diff}}/E_b = 0.4$ ’ (dashed line) chemical models and grain-surface (ice) CH₃OH vertical column density in the ‘ $E_{\text{diff}}/E_b = 0.4$ ’ model divided by 10^7 (dotted line).

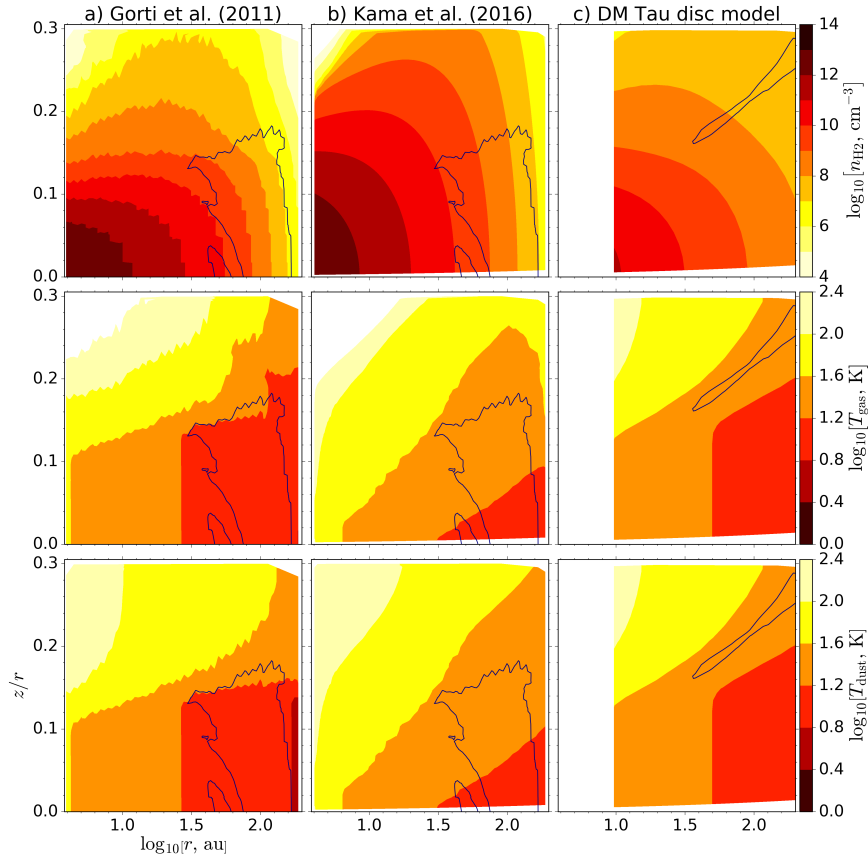


Figure 3. TW Hya and DM Tau disc models. Left and middle columns show relative methanol abundances (wrt H₂) computed with the physical models of [Gorti et al. \(2011\)](#) and [Kama et al. \(2016\)](#), respectively. Right column shows the methanol abundances computed with the DM Tau disc model taken from [Semenov & Wiebe \(2011\)](#). The black contours denote the methanol abundance of 10^{-12} .

this averaging affects the synthetic spectra following the procedure given by [Cleeves et al. \(2016\)](#). We performed calculations of the synthetic spectra with a spectral resolution of 0.015 km s^{-1} , ten times higher than our initial resolution and the resolution of the W16 data, before averaging the results of these computations back to the resolution of 0.15 km s^{-1} . The resulting synthetic peak line flux densities do not vary by more than 3 per cent due to the averaging, a variation which is significantly lower than the ratio of the rms noise (6.5 mJy) to the peak flux density (33 mJy) in the spec-

trum of W16. Thus we assume the averaging can safely be neglected.

W16 considered the Band 7 $2_1 - 2_0 A^{++}$ (304.208 GHz), $3_1 - 3_0 A^{++}$ (305.473 GHz), $4_1 - 4_0 A^{++}$ (307.166 GHz) transitions (hereafter, B7 lines) and Band 6 $5_0 - 4_0 E$ (241.700 GHz), $5_{-1} - 4_{-1} E$ (241.767 GHz), $5_0 - 4_0$ (241.791 GHz) transitions (hereafter, B6 lines). The difference in the maximum specific intensity of the synthetic images for these lines between the ‘ $E_{\text{diff}}/E_b = 0.77$ ’ and ‘ $E_{\text{diff}}/E_b = 0.4$ ’ models does not exceed 45 per cent. The

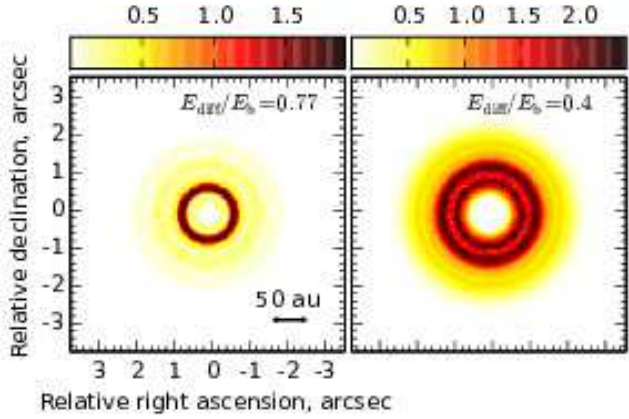


Figure 4. The zeroth moment maps obtained for the $3_1 - 3_0 A^{++}$ (305.473 GHz) transition with the ‘ $E_{\text{diff}}/E_b = 0.77$ ’ (left panel) and ‘ $E_{\text{diff}}/E_b = 0.4$ ’ (right panel) disc chemical models. The colour bars denote the intensity in 10^{-6} Jy pixel $^{-1}$ km s $^{-1}$.

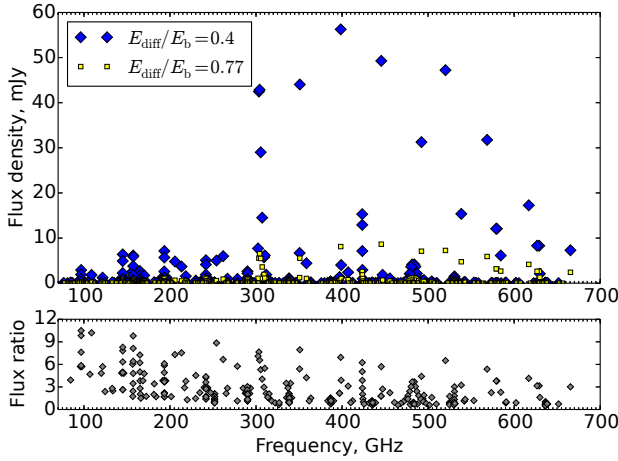


Figure 5. The synthetic spectra computed with the LIME code. Upper panel shows the line peak flux densities of CH₃OH calculated for the ‘ $E_{\text{diff}}/E_b = 0.77$ ’ and ‘ $E_{\text{diff}}/E_b = 0.4$ ’ TW Hya disc chemical models. Lower panel shows the ratio of line peak flux densities in the ‘ $E_{\text{diff}}/E_b = 0.77$ ’ and ‘ $E_{\text{diff}}/E_b = 0.4$ ’ models.

spatial distribution of the CH₃OH emission, however, is significantly different, primarily caused by the difference in the methanol column densities N_M between the models (see Sect. 2). In the case of the ‘ $E_{\text{diff}}/E_b = 0.77$ ’ model, the CH₃OH emission is mainly concentrated within a thin ring, while in the case of the ‘ $E_{\text{diff}}/E_b = 0.4$ ’ model it is distributed over a larger image area (see Fig. 4).

The line flux densities, F_ν , in the spectra obtained with the ‘ $E_{\text{diff}}/E_b = 0.77$ ’ model are lower by a factor of < 9 than those obtained with the ‘ $E_{\text{diff}}/E_b = 0.4$ ’ model (see Fig. 5). The difference in F_ν between the two chemical models increases with increasing F_ν and with decreasing transition frequency.

The synthetic LTE CH₃OH spectra do not differ by more than a factor of 3.5 from the non-LTE spectra for both the ‘ $E_{\text{diff}}/E_b = 0.77$ ’ and ‘ $E_{\text{diff}}/E_b = 0.4$ ’ models (see Fig. 6). For the strongest lines with $F_\nu > 10$ mJy, the LTE fluxes do not exceed the non-LTE fluxes by more than 30 per cent, while the largest deviations from LTE occur for the $J_2 \rightarrow J_1 A$ and $J_{-2} \rightarrow J_{-1} E$ line series. The emission dis-

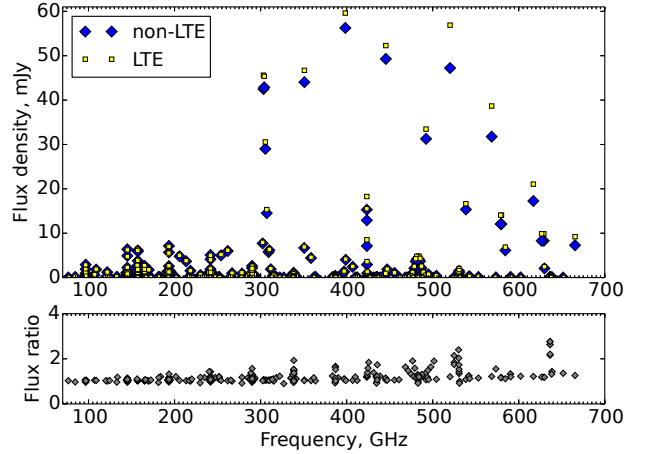


Figure 6. The synthetic spectra calculated with LIME code for the ‘ $E_{\text{diff}}/E_b = 0.4$ ’ TW Hya disc chemical model. Upper panel shows the line peak flux densities of CH₃OH in LTE and non-LTE synthetic spectra. Lower panel shows the ratio of LTE and non-LTE line peak flux densities. Only lines with peak flux densities > 0.01 mJy are shown.

tribution in the synthetic images is similar in both LTE and non-LTE cases. This is in contrast to our previous study (Parfenov et al. 2016), where we used the DM Tau disc model, and where the majority of methanol lines were found to be sub-thermally excited and had intensities well below their LTE intensities. This discrepancy is due to the adopted disc density structures, where the current model of the TW Hya disc is denser than the previous DM Tau model (see Figure 3). Moreover, in the case of the DM Tau disc, gas-phase methanol resides mainly in the upper disc layers with lower densities compared to the TW Hya disc. Higher gas densities in the TW Hya model lead to the thermalization of most of the low-energy methanol transitions.

The peak LTE fluxes in B6 and B7 transitions do not differ from the non-LTE ones by more than 8 per cent, a factor of a few lower than the ratio of the noise to the signal in the W16 spectrum. Thus, due to relatively small influence of non-LTE effects on the intensity of B6 and B7 lines, the synthetic images used to simulate the W16 observations in Section 4 were calculated assuming LTE. To minimize artefacts caused by finite resolution and randomness of the LIME spatial grid we averaged images obtained with 10 different grid realizations. These averaged images were used as input models for the simulations of W16 observations in Section 4.

We have also tested how the optical depth decrease observed in the disc gaps can influence the LRT results. For this purpose, we varied the gas-to-dust ratio keeping the gas density fixed to reproduce the optical depth variations across the gaps estimated by Tsukagoshi et al. (2016). We have considered the two most prominent gaps at 22 and 37 au from the disc centre and modelled them as Gaussians with a full width at half maximum of 3 au and a depth of 0.25. We did not find any significant influence of the gaps on the modelled disc spectra and images. The spectra obtained with and without gaps do not differ by no more than 8 per cent. The variations of F_ν of B7 and B6 lines due to gaps do not exceed 1 per cent and are thus negligible. It should be noted also that (sub-)mm continuum observations of the TW Hya disc indicate that the spatial distribution of the mm-sized grains

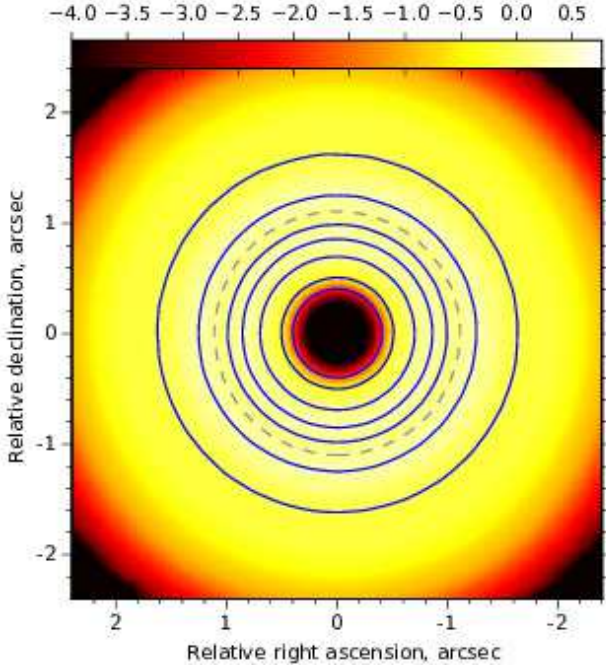


Figure 7. The zeroth moment map obtained for the $3_1 - 3_0 A^+$ (305.473 GHz) transition with the ‘ $E_{\text{diff}}/E_b = 0.4$ ’ disc chemical model. The colour bar denotes the \log_{10} of intensity in 10^{-6} Jy pixel $^{-1}$ km s $^{-1}$. Solid contour lines denote the ratio of the maximum CH₃OH line specific intensity calculated with zero dust opacity to the line specific intensity calculated with the Menu et al. (2014) dust opacity. The contours from outer to inner are 1.01, 1.1, 1.3, 1.5, 2, 4 and 8. Dashed grey line shows the radius of 66 AU outside which the large grains are depleted according to the (sub-)mm continuum observations of the TW Hya disc by (Andrews et al. 2012).

in the disc has a sharp outer cutoff (Andrews et al. 2012; Hogerheijde et al. 2016). Assuming the distance to TW Hya of 54 pc, Andrews et al. (2012) estimated that this cutoff is located at $r = 60$ au which translates to 66 au for the distance of 59.5 pc. The Gorti et al. (2011) and Kama et al. (2016) disc models do not have such a cutoff in their grain populations. Our test LRT calculations with zero dust opacity show that the CH₃OH line specific intensities in our model decrease by no more than 25 per cent due to non-zero dust (sub-)mm opacities at $r > 66$ au, compared with the case when the dust opacity is absent at $r > 66$ au (see Fig. 7). The peak flux density increase due to absence of the dust opacity at $r > 66$ au does not exceed 5 per cent and thus can be neglected.

4 SIMULATION OF ALMA OBSERVATIONS.

The simulations of the TW Hya disc observations were performed with the SIMOBSERVE and SIMANALYZE tasks of the CASA package version 4.7.0. The parameters of these tasks were chosen to provide the parameters of simulated observations as close as possible to observations of W16. This resulted in synthesized line beams that are $1.''3 \times 0.''8$ (PA = -80°) and $0.''6 \times 0.''5$ (PA = -89°) for the B7 and B6 data, respectively. To perform the uv-stacking of individual transitions within the B7 and B6 datasets we used the

same values for the SIMOBSERVE input frequency of 305.5 and 241.7 GHz, respectively. As in W16, we imaged the line data without CLEANing. The rms noise level in the resulting channel maps for B6 and B7 lines is ~ 4.5 mJy beam $^{-1}$. The continuum data at 317 GHz were imaged and CLEANed down to a 0.2 mJy beam $^{-1}$ threshold using Briggs weighting.

CH₃OH emission was not detected in all our channel maps for individual lines except in the channel maps for the $2_1 - 2_0 A^+$ transition (304.208 GHz) calculated with the ‘ $E_{\text{diff}}/E_b = 0.4$ ’ chemical disc model. The emission in this transition was detected at the level of $\gtrsim 3\sigma$ in six velocity channels at 2.45, 2.6, 2.75, 3.05, 3.2 and 3.35 km s $^{-1}$. Following W16, we also performed stacking of visibility data for individual lines within B6 and B7 datasets. We stacked, imaged and CLEANed B6 and B7 data using the CLEAN task with natural weights. An rms noise level in the resulted stacked data for B6 and B7 lines is ~ 2.2 mJy beam $^{-1}$. A significant signal is only present in stacked B7 data calculated using the ‘ $E_{\text{diff}}/E_b = 0.4$ ’ chemical model. The CH₃OH emission is detected at the level of $\gtrsim 3\sigma$ in seven velocity channels from 2.45 to 3.35 km s $^{-1}$ (see Fig. 8).

The methanol emission in our stacked B7 data appears as a ring around the disc centre with a radius of ~ 1.1 arcsec (60 au). The peak flux in the spectrum obtained by spatial integration of the line emission within 3σ contour of the 317 GHz continuum is ~ 37 mJy. Taking into account the rms noise of 6.7 and 6.5 mJy in the spectra of ours and W16 results respectively, the peak integrated flux density of 37 mJy is equal to the peak integrated flux density of 33 mJy obtained by W16.

The LIME images in B7 lines obtained by us using the Gorti et al. (2011) physical model coupled with the best ‘by-eye’ fit chemical model of W16 were stacked by simple averaging. The peak integrated flux density in this stacked data is 28 or 34 mJy depending on whether Menu et al. (2014) or Andrews et al. (2011) dust opacities are utilized, respectively. This is 5 mJy within the synthetic $F_\nu = 33$ mJy obtained by W16 with the Kama et al. (2016) physical model. Thus the difference in flux densities estimated with the same CH₃OH distribution but with the two different yet feasible TW Hya disc physical models does not exceed the rms noise in both our spectra and the spectra of W16. We conclude that the differences in the disc physical models do not affect significantly the results of our simulations.

5 DISCUSSION AND CONCLUSIONS

The adopted chemical disc model has a complexity comparable to other contemporary disc chemical models. Along with an appropriate TW Hya disc physical structure this chemical model is able to reproduce the W16 CH₃OH detection rather well. Our model predicts a CH₃OH abundance that is lower by about two orders of magnitude in comparison with other T Tauri disc chemical studies with similar models. The reason for such a discrepancy is mainly due to the difference in the adopted disc physical structures rather than the chemical models. Indeed, the TW Hya disc is more compact and dense compared to the disc models used by e.g. Willacy (2007); Semenov & Wiebe (2011); Walsh et al. (2014); Furuya & Aikawa (2014).

The CH₃OH abundance on the grain surfaces predicted

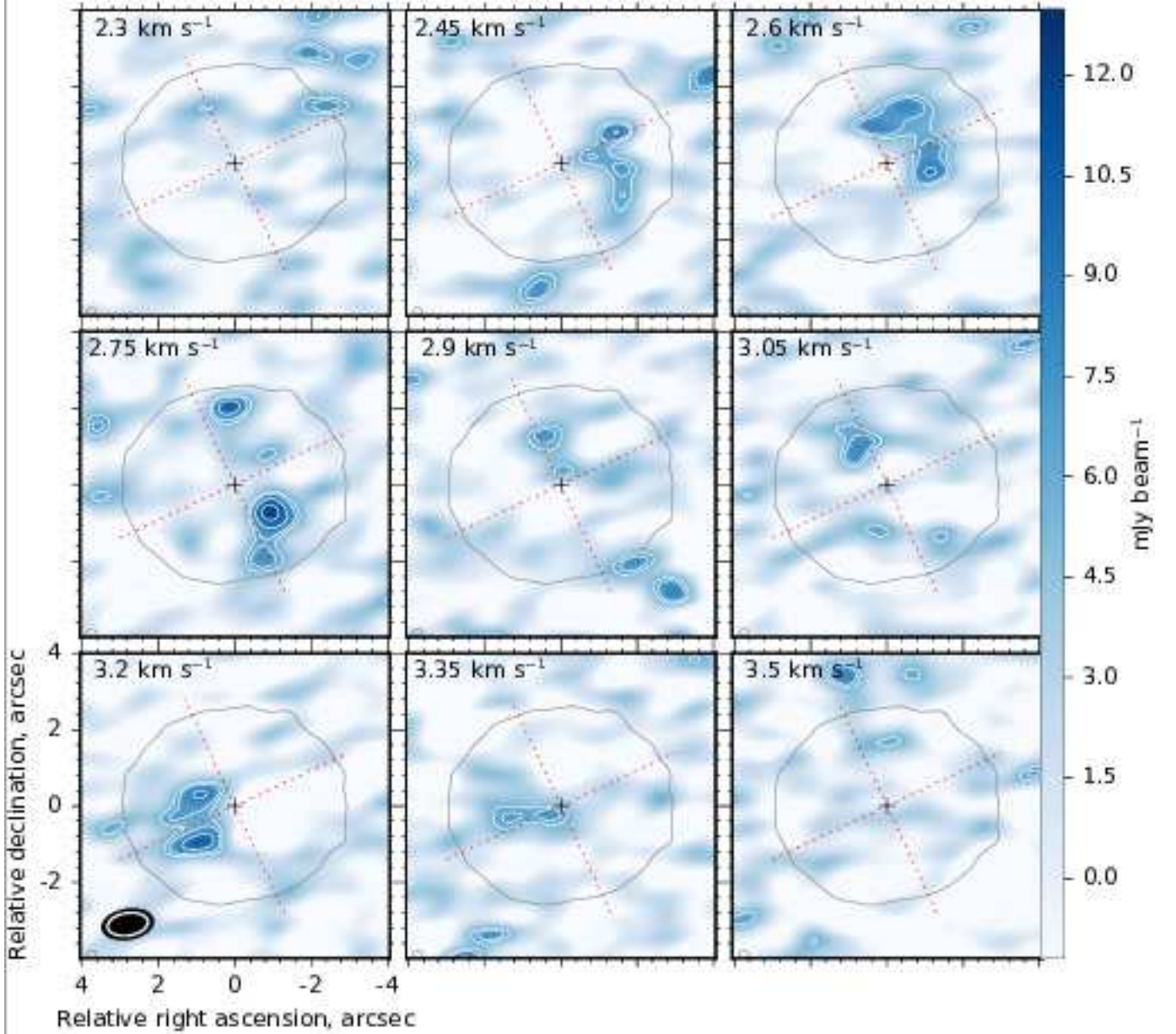


Figure 8. The synthetic channel maps for the stacked B7 data calculated with the ‘ $E_{\text{diff}}/E_b = 0.4$ ’ TW Hya disc chemical model. White contours show 2.5σ , 3σ , 4σ and 5σ levels for the B7 data. Grey contour shows the 3σ level of continuum emission at 317 GHz. Dashed lines denote minor and major disc axes and the black cross denotes the stellar position. The synthesized beams for the continuum and line data are shown as open white and filled black ellipses, respectively.

with our TW Hya disc model is relatively high and comparable with the estimates of [Walsh et al. \(2014\)](#) (see Fig. 2). Methanol ice in our TW Hya disc model reaches its highest concentrations at around 30–50 au from the disc centre, where the temperatures in the disc mid-plane are most favourable for CO hydrogenation on grain surfaces. One of the main formation routes of gas-phase methanol in our model is the photodesorption of methanol ice by interstellar UV photons and UV photons produced by CRP excitation of H_2 . The effectiveness of the UV photodesorption in dense discs is restricted to layers well above the disc mid-plane. In contrast, CRPs and partly attenuated, very hard X-ray pho-

tons are able to penetrate larger gas columns and are able to maintain a relatively high gas-phase CH_3OH abundance in the molecular layers adjacent to the mid-plane. The maximum of the CH_3OH gas-phase abundance does not coincide with the one of methanol ice. This is related with high gas and dust density in the disc regions at $r < 50$ au leading to a low efficiency of CH_3OH ice desorption in comparison with corresponding freeze out timescales. At larger radii, where the disc becomes less dense and more transparent to the interstellar UV radiation and freeze out of gas-phase CH_3OH is slower, the CH_3OH gas-phase abundance increases and reaches its maximum, leading to the appearance of a ring of

methanol emission with a radius of ~ 60 au. This also explains why the ring of methanol emission in our model does not coincide with the CO snow line located at ~ 30 au from the TW Hya disc centre (Qi et al. 2013).

The TW Hya disc physical structure is also responsible for relatively small deviations from LTE in CH_3OH transitions. For the strongest CH_3OH transitions, including those observed by W16, the critical density is lower than the gas density by a factor of > 10 throughout most of the disc regions with a relatively high ($X_{\text{M}} > 10^{-12}$) methanol abundance. This is in contrast to the predictions of Parfenov et al. (2016) based on the DM Tau disc model, according to which LTE and non-LTE CH_3OH line flux densities can differ by up to two orders of magnitude. Thermalization of the strongest methanol transitions in the TW Hya disc makes them a reliable probe of the disc thermal structure. The strong transitions with $F_{\nu} > 10$ mJy that show maximum deviations from LTE occur in the frequency range of 500–600 GHz and can not be accessed with ALMA due to a frequency gap between ALMA Bands 8 and 9.

In this study, we have used the TW Hya disc physical model of Gorti et al. (2011) that is different from the model of Kama et al. (2016). This difference can be considered as an uncertainty in TW Hya disc physical parameters. Our calculations have shown that this uncertainty does not affect significantly the results of LRT calculations. We also expect that this uncertainty does not affect the CH_3OH distribution in the disc. The methanol line flux densities are much more sensitive to the uncertainties of the disc chemical model.

One of the main parameters of chemical models that influence the abundances of complex species is $E_{\text{diff}}/E_{\text{b}}$ (see e.g. Walsh et al. 2014). In this study, we considered the models with $E_{\text{diff}}/E_{\text{b}} = 0.4$ and 0.77 which are close to the extreme values adopted in chemical studies. The former model is consistent with the observations while the latter model underpredicts the line flux densities by a factor of several compared to the W16 observations. The influence of other chemical model parameters like the probability of chemical desorption as well as physical parameters like the dust grain size distribution is a subject for future studies.

ACKNOWLEDGEMENTS

We thank an anonymous referee for providing valuable suggestions to improve this paper. S. Parfenov, A. Sobolev and A. Shapovalova are financially supported by the Russian Science Foundation (project no. 15-12-10017). DAS acknowledges support from the Heidelberg Institute of Theoretical Studies for the project "Chemical kinetics models and visualization tools: Bridging biology and astronomy". This research made use of NASA's Astrophysics Data System. The figures in this paper were constructed with the MATPLOTLIB package (Hunter 2007) and APLPY package hosted at <http://aplpy.github.io>.

REFERENCES

Aikawa Y., Momose M., Thi W.-F., van Zadelhoff G.-J., Qi C., Blake G. A., van Dishoeck E. F., 2003, *PASJ*, **55**, 11

- Andrews S. M., Wilner D. J., Espaillat C., Hughes A. M., Dullemond C. P., McClure M. K., Qi C., Brown J. M., 2011, *ApJ*, **732**, 42
- Andrews S. M., et al., 2012, *ApJ*, **744**, 162
- Andrews S. M., et al., 2016, *ApJ*, **820**, L40
- Bergin E. A., Blake G. A., Ciesla F., Hirschmann M. M., Li J., 2015, *Proceedings of the National Academy of Science*, **112**, 8965
- Bertin M., et al., 2016, *ApJ*, **817**, L12
- Biver N., et al., 2015, European Planetary Science Congress 2015, held 27 September - 2 October, 2015 in Nantes, France, Online at http://meetingorganizer.copernicus.org/EPSC2015/EPSC2015">id.EPSC2015-503, **10**, EPSC2015
- Brinch C., Hogerheijde M. R., 2010, *A&A*, **523**, A25
- Bruderer S., 2013, *A&A*, **559**, A46
- Calvet N., D'Alessio P., Hartmann L., Wilner D., Walsh A., Sitko M., 2002, *ApJ*, **568**, 1008
- Caselli P., Ceccarelli C., 2012, *A&ARv*, **20**, 56
- Chapillon E., et al., 2012, *ApJ*, **756**, 58
- Ciesla F. J., Sandford S. A., 2012, *Science*, **336**, 452
- Cleeves L. I., Öberg K. I., Wilner D. J., Huang J., Loomis R. A., Andrews S. M., Czekala I., 2016, *ApJ*, **832**, 110
- Cridland A. J., Pudritz R. E., Alessi M., 2016, *MNRAS*, **461**, 3274
- Cruz-Diaz G. A., Martín-Doménech R., Muñoz Caro G. M., Chen Y.-J., 2016, *A&A*, **592**, A68
- Cuppen H. M., Walsh C., Lamberts T., Semenov D., Garrod R. T., Penteado E. M., Ioppolo S., 2017, *Space Sci. Rev.*,
- Debes J. H., Jang-Condell H., Weinberger A. J., Roberge A., Schneider G., 2013, *ApJ*, **771**, 45
- Drozdovskaya M. N., Walsh C., Visser R., Harsono D., van Dishoeck E. F., 2014, *MNRAS*, **445**, 913
- Ducourant C., Teixeira R., Galli P. A. B., Le Campion J. F., Krone-Martins A., Zuckerman B., Chauvin G., Song I., 2014, *A&A*, **563**, A121
- Fray N., et al., 2016, *Nature*, **538**, 72
- Furuya K., Aikawa Y., 2014, *ApJ*, **790**, 97
- Gaia Collaboration et al., 2016, *A&A*, **595**, A2
- Gorti U., Hollenbach D., Najita J., Pascucci I., 2011, *ApJ*, **735**, 90
- Gürtler J., Klaas U., Henning T., Abraham P., Lemke D., Schreyer K., Lehmann K., 2002, *A&A*, **390**, 1075
- Henning T., Semenov D., 2013, *Chemical Reviews*, **113**, 9016
- Herbst E., van Dishoeck E. F., 2009, *ARA&A*, **47**, 427
- Hogerheijde M. R., Bekkers D., Pinilla P., Salinas V. N., Kama M., Andrews S. M., Qi C., Wilner D. J., 2016, *A&A*, **586**, A99
- Hunter J. D., 2007, *Computing In Science & Engineering*, **9**, 90
- Kalenskii S. V., Sobolev A. M., 1994, *Astronomy Letters*, **20**, 91
- Kama M., et al., 2016, *A&A*, **592**, A83
- Menu J., et al., 2014, *A&A*, **564**, A93
- Mordasini C., Alibert Y., Klahr H., Henning T., 2012a, *A&A*
- Mordasini C., Alibert Y., Georgy C., Dittkrist K.-M., Klahr H., Henning T., 2012b, *A&A*
- Mordasini C., van Boekel R., Mollière P., Henning T., Benneke B., 2016, *ApJ*, **832**, 41
- Öberg K. I., Guzmán V. V., Furuya K., Qi C., Aikawa Y., Andrews S. M., Loomis R., Wilner D. J., 2015, *Nature*, **520**, 198
- Parfenov S. Y., Semenov D. A., Sobolev A. M., Gray M. D., 2016, *MNRAS*, **460**, 2648
- Qi C., et al., 2004, *ApJ*, **616**, L11
- Qi C., et al., 2013, *Science*, **341**, 630
- Schöier F. L., van der Tak F. F. S., van Dishoeck E. F., Black J. H., 2005, *A&A*, **432**, 369
- Semenov D., Wiebe D., 2011, *ApJS*, **196**, 25
- Semenov D., Wiebe D., Henning T., 2004, *A&A*, **417**, 93
- Semenov D., et al., 2010, *A&A*, **522**, A42
- Sutton E. B., Sobolev A. M., Salii S. V., Malyshev A. V., Ostrovskii A. B., Zinchenko I. I., 2004, *ApJ*, **609**, 231

- Teague R., et al., 2017, [ApJ](#), **835**, 228
Tsukagoshi T., et al., 2016, [ApJ](#), **829**, L35
Vasyunin A. I., Semenov D., Henning T., Wakelam V., Herbst E., Sobolev A. M., 2008, [ApJ](#), **672**, 629
Walsh C., Millar T. J., Nomura H., Herbst E., Widicus Weaver S., Aikawa Y., Laas J. C., Vasyunin A. I., 2014, [A&A](#), **563**, A33
Walsh C., et al., 2016, [ApJ](#), **823**, L10
Willacy K., 2007, [ApJ](#), **660**, 441
Winn J. N., Fabrycky D. C., 2015, [ARA&A](#), **53**, 409
van Boekel R., et al., 2016, preprint, ([arXiv:1610.08939](#))

This paper has been typeset from a \TeX / \LaTeX file prepared by the author.